
ANALYSIS OF FUNCTIONAL NEURAL CODES OF DEEP LEARNING MODELS: FUNCTIONAL TELESCOPE HYPOTHESIS

A PREPRINT

Jung H. Lee
Pacific Northwest National Laboratory
Seattle, WA
jung.lee@pnnl.gov

Sujith Vijayan
School of Neuroscience
Virginia Tech
Blacksburg, VA
neuron99@vt.edu

November 28, 2023

ABSTRACT

Deep neural networks (DNNs), the agents of deep learning (DL), require a massive number of parallel/sequential operations, which makes it difficult to comprehend their operations and impedes proper diagnosis. Without better knowledge of DNNs' internal process, deploying DNNs in high-stakes domains can lead to catastrophic failures. Therefore, to build more reliable DNNs/DL, it is imperative that we gain insights into their underlying decision-making process. Here, we use the self-organizing map (SOM) to analyze DL models' internal codes associated with DNNs' decision-making. Our analyses suggest that shallow layers close to the input layer compress features into condensed space and that deep layers close to the output layer expand feature space. We also found evidence indicating that compressed features may underlie DNNs' vulnerabilities to adversarial perturbations.

1 Introduction

Deep learning (DL) can train DL models (deep neural networks, DNNs) with examples to perform a wide range of real-world problems [1, 2, 3]. This may remove the need for human experts' instructions, but DL models depend on a large number of linear and nonlinear operations, making their operations incomprehensible. If we do not understand their operations, we cannot conduct timely predictions of failures or perform proper diagnosis, and without proper diagnosis, we cannot safely deploy DNNs in the real world [4, 5]. Furthermore, DL remains vulnerable to adversarial perturbations, imperceptible changes crafted to disrupt DL models' decisions-making process [6, 7, 8].

Therefore, to utilize DL's capability in high-stakes domains, we need to understand how DNNs make or reach their decisions. As DNNs successively transform inputs into final predictions, probing hidden layers' responses can shed light on DNNs' operations. Earlier studies showed that shallow layers (i.e., layers close to the input layer) encode simple low-level features, whereas deep layers (i.e., layers close to the output layer) encode high-level features [9, 10, 11]. The high level features sometimes include human interpretable features. Notably, the low-level features in the shallow layers resemble the features, to which biological neurons in the early stage of visual systems would respond [12].

Then, two important questions arise. How do individual layers evolve? And how do they contribute to DNNs' decisions? Multiple studies have been dedicated to answer these questions, which has led to a subfield of DL named 'explainable AI'. The studies can fall into three categories. The first line of studies estimated inputs' influence on DNNs' decisions. Specifically, several studies utilized gradient-based analysis [13, 14, 15], the layerwise relevance propagation that assigned individual neurons' relevance using backpropagation-like rules [16] and occlusion analysis that measured input patches' influence [10]. The second line of studies focused on analyzing hidden layer representations. The feature visualization [17, 11] inverted DNNs to identify optimal features that can drive certain hidden layers. Testing with concept activation vectors (TCAV) used examples with and without human-annotated concepts to train a secondary model to learn concept vectors [18]. Once the secondary model is trained, it can evaluate the influence of concept vectors

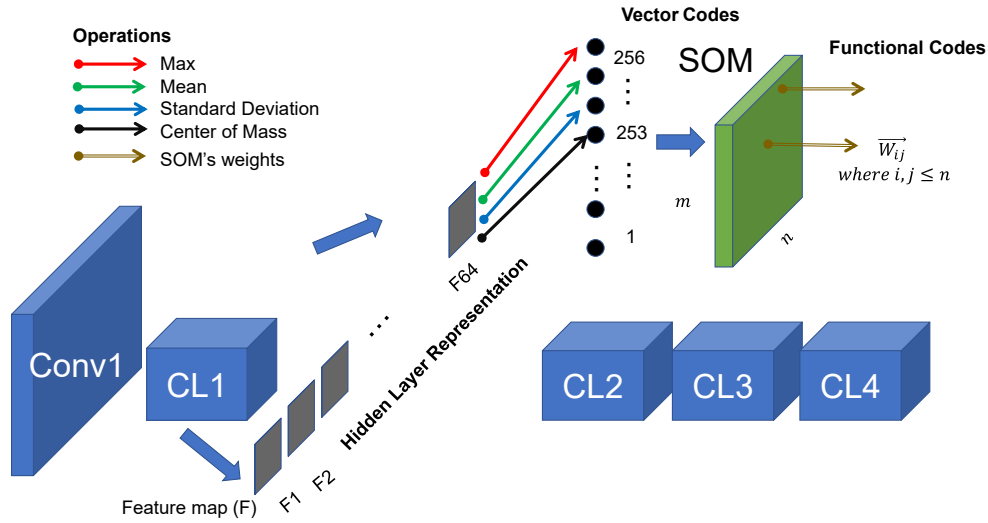


Figure 1: Schematics of SOM-based analysis. We display ResNet18 as an example. The same approach is applied to ResNet50, VGG19 and DenseNet121. We convert individual feature maps’ responses to vector codes using max, mean, standard deviation and center of mass. Vector codes are abstract representations of feature map outputs (hidden layer representations) and are inputs to a SOM, which identifies functional codes.

on DL models. Finally, the third line of studies evaluated direct relationships between hidden layer representations and DNNs’ decisions [19, 20].

Here, to better understand the functional codes underlying DNNs’ operations, we used unsupervised learning to analyze hidden layer representations. Our study is based on the assumption that the number of functional codes is much smaller than the dimension of input feature space, and the mapping between inputs and functional codes should be many-to-one. If each input can be mapped onto a unique functional code, DNNs can effectively become memory cells that do not generalize their predictions on unknown inputs (queries). We also assumed that functional codes would appear repeatedly during DNNs’ operations. With these assumptions in mind, we used the self-organizing map (SOM) [21, 22], an unsupervised learning algorithm, to probe hidden layer representations. Our analyses suggest that shallow layers in DNNs map inputs to extremely homogeneous codes, while deep layers map inputs to more diverse codes. This reminded us of the fact that convex and concave lenses in telescopes collect light and enhance images’ resolution. We further found evidence suggesting that the homogeneous functional codes in the shallow layers may underlie DL’s vulnerabilities to adversarial perturbations.

2 Approach

In principle, DNNs are trained to generate many-to-one mappings. For instance, classifiers are trained to map high dimensional inputs into a small number of classes. Based on the fact DL models contain identical functional blocks in series, we hypothesize that internal modules of DL models may also produce many-to-one like mappings. More specifically, we hypothesize that 1) a group of inputs is mapped onto the same internal code in a hidden layer, and 2) the memberships of functional groups mapped onto the same internal codes depend on layers. For instance, inputs A and B can be mapped onto the same code in layer n , but inputs A and B are not necessarily mapped onto the same code in layer m .

This hypothesis has an important implication for explainable DL. If we decode such internal many-to-one like mappings, we can use them to decompose DL models’ decisions into functional components. Inspired by the brain’s grandmother cells, we argue that these functional components can correspond to the concepts in the brain. Then, how can we confirm or reject this hypothesis? If many-to-one like mappings are internally created and used for DL models’ functions, internal codes in hidden layers will be grouped together. Thus, we need to ask if hidden layer codes/representations are grouped together, and if they are not grouped together, we can reject this hypothesis. In our study, we use self-organizing map (SOM), an unsupervised learning algorithm, to test the hidden layer codes.

We refer to raw hidden layer outputs as ‘hidden layer representations’, which are known to be highly variable and sensitive to input pixel intensities. We refer to internal representations as ‘functional codes’, which mediate semantic meanings of inputs. To discover functional codes used by DL models, we first convert hidden layer representations into more abstract vector codes by characterizing feature maps’ outputs with their statistical properties.

2.1 Vector Codes of feature maps

Convolution filters produce 2-dimensional outputs (feature maps), which reflect the spatial distribution of inputs. In modern DNNs, dimensions of all the features produced by these filters are often too big. If we take activations of all feature maps by flattening them into 1D vectors, the final vectors reflecting individual layers can contain a great amount of stochastic noise, making the analysis overly sensitive to statistical fluctuation or biases that may be irrelevant to semantic information of inputs. Earlier studies employed various dimension reduction algorithms to analyze features; see [23, 24, 19] for example. Specifically, Alain and Bengio [19] used two dimension reduction methods. First, responses were randomly sampled from a subset of spatial locations of feature maps. This ‘random sampling’ was also used by other studies [23, 24]. Second, 2D pooling was used to reduce the number of features to the number of channels. We note that random sampling or naive 2D pooling can result in some crucial information of inputs to be lost, especially in shallow layers, in which feature maps have large spatial dimensions (both height and width). To minimize the loss of information, we coded the individual feature maps by taking max, mean, standard deviation and center of mass of activations (Fig. 1), which may help us partially preserve spatial information of the feature maps and make our analysis insensitive to some stochastic/spurious noises independent of inputs’ semantic meanings. These abstract codes will be referred to as vector codes below.

2.2 Identification of functional codes

We assume that internal representations can be decomposed into functional codes and noise, and noises can be averaged out by native operations (e.g., summations/convolutions) occurring inside DNNs. As SOM [21, 22] can identify representative inputs and their relationships in high dimensional feature space, we used it to identify effective functional codes from vector codes. Fig. 1 illustrates our experiment procedure. We first recorded hidden layer representations to obtain vector codes and then trained a SOM on vector codes to identify functional codes.

In this study, we analyzed four popular ImageNet models, ResNet18, ResNet50 [25], DenseNet121 [26] and VGG19 [27]. Modern DL models consist of composite blocks. For instance, ResNets consist of 4 composite blocks ([25]), which will be referred to as the composite layer (CL) below (Fig. 1). Similarly, DenseNet121 and VGG19 also have functional blocks naturally corresponding to ResNet’s CLs. As these functional blocks can represent early, middle and late processing stages, we analyzed functional codes in them using Timm, an open source pytorch library [28] and its feature extractor API. Specifically, we obtained hidden layer representations from examples randomly chosen from ImageNet [29]. Then, hidden layer representations were converted to 1-dimensional vector codes using max, mean, standard deviation and center of mass. Following this rule, the dimension of the vector codes are 4 times bigger than the number of channels. For instance, we obtained 256, 512, 1024, 2048-dimensional vector codes from ResNet18. In this study, we used 4 first functional blocks for all 4 models; see Timm [28] for more details on all 4 models.

2.3 SOM and its training to determine functional codes

SOM consists of units distributed over 2-dimensional grids [21, 22]. Each unit stores a single weight vector, whose length is the same as that of an input. During training, each input is compared to the weights stored in the units, and the best matching unit (BMU) is identified. Then, the weight of BMU and its neighbors are updated according to the learning rule (Eq. 1).

$$W_v(s+1) = W_v(s) + \exp\left(-\frac{D^2}{2\sigma(s)^2 + \epsilon}\right) \times \alpha(s) \times (x - W_v(s)) \quad (1)$$

, where s denotes training index; u and v denote the best matching unit (BMU) and a unit to be updated, respectively; where W denotes a weight; where α is a learning rate; x is an input; where $D = \|x - W_u\|$, distance metric; ϵ is added for numerical stability.

With this update rule, SOM’s weights move towards inputs but the degree of changes depend on the location of the units. BMU or its neighboring units update weights strongly, but units far from BMU update them less strongly. Notably, SOM has two properties. First, the weights of SOM tend to be similar to the inputs and represent exemplary inputs after training. Second, the neighboring units store similar weights, and consequently the distance between BMUs reflects the similarity between the inputs. That is, after training, the similarity between the two inputs can be measured with the distance between their corresponding BMUs. We used these properties to analyze functional codes.

We used two sets of 50,000 inputs randomly drawn from ImageNet [29]. The first set (SOM-tr) was built with the ImageNet train set, and the second set (SOM-val), with the ImageNet validation set. Both sets contain 50 examples per each ImageNet class. Only SOM-tr was used to train SOMs, and SOM-val was used to probe their responses to unseen examples. For individual inputs from the two sets, we obtained vector codes from 4 CLs of ResNets and grouped them according to layers (i.e., CL). The vector codes from the same layer were used to train and test a SOM. As there are 4 CLs, we built and trained 4 independent SOMs. A wide range of distance metrics have been used for SOMs in the earlier studies, and we selected the cosine distance (CD, Eq. 2) to measure the similarity between SOMs’ weights and a vector code. SOMs were constructed with the periodic boundary to avoid boundary effects observed during training. With the periodic boundary condition, SOM effectively became a 2-dimensional torus, and the distance was measured accordingly.

$$CD(u, v) = 1 - \frac{u \cdot v}{\|u\| \|v\|} \quad (2)$$

We used an open source python library QuickSOM [30] to construct SOM with a square grid. In the experiment, we tested SOMs of 4 different sizes. They contained 10-by-10, 20-by-20, 30-by-30 or 40-by-40 nodes at square grids. As we did not observe significant dependency on SOMs’ sizes, the analyses below are based on SOMs consisting of 20-by-20 units, unless stated otherwise. table 1 shows the hyperparameters selected for the experiments, and the terminologies are adopted from QuickSom.

Table 1: We list the parameters selected for SOM. m and n denote the height and width, respectively. In the experiment, we used a square grid ($m = n$). σ and α denotes their initial values, and they decay over time. We used ‘exp’ decay mode supported by Quicksom [30]

Parameter	value
m (height)	10,20,30,40
n (width)	10,20,30,40
σ	10
α	0.1
decay	exp

2.4 Analysis of functional codes

After training, we considered the weights of trained SOMs as effective functional codes of DL models (Fig. 1) and used them to address two questions. First, can SOMs learn functional codes? In other words, can the weights of SOMs mediate semantic meanings of inputs (in our analysis, the labels of inputs)? Second, what properties do functional codes in 4 CLs have? Regarding the first question, we obtained top-10 BMUs corresponding to individual vector codes elicited by images in SOM-tr and SOM-val and grouped them according to inputs’ labels. If SOMs learn functional codes, BMUs corresponding to the vector codes elicited by the same class inputs would be close to one another. For the second question, we studied BMUs’ relationships to one another by measuring the Euclidean distance between BMUs and CD (Eq. 2) between their weights.

As a constructed SOM is a torus (due to the periodic boundary condition), we measured the shortest distance between SOMs’ nodes in a torus. Specifically, the trained SOM was mapped onto the center of 9 grids. When we estimated Euclidean distance between the two SOM units, one of the two units was mapped onto the center grid, and another, onto one of 9 grids (Fig. 2A), in which the shortest distance is available. In our analysis, we also identified the class centers using SOM’s BMUs. In doing so, for each class, we first determined which unit was frequently chosen as BMU while the same class inputs from SOM-tr were fed to ImageNet models. Then, all BMUs of the same class examples were mapped onto one of 9 grids (Fig. 2A), in which the distances to the most frequently chosen BMU were the shortest. The class center is the center of BMUs’ mass. in this unfolded SOM (see the bottom row of Fig. 2B for examples).

3 Results

We first ask if vector codes can be decomposed into effective low-dimensional components by using the principle component analysis (PCA) analysis on vector codes from CL1, 2, 3 and 4 of ResNet18, ResNet50, DenseNet121 and VGG19. Fig. 3A-D show the explained variance (EV) of top 30 principal axes. As shown in the figures, EV in CL1 increases quite rapidly, as the number of principal axes grows. The growth rate of EV is substantially smaller in the deep layers, especially in CL3 and CL4. This result supports that inputs can be mapped onto a finite number of internal codes.

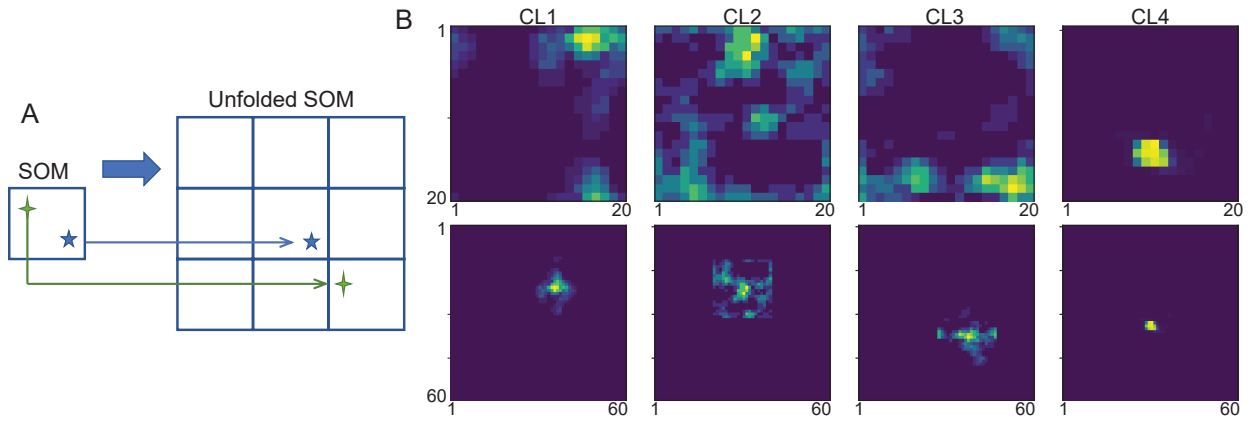


Figure 2: Unfolding SOM. When Euclidean distances between two SOM units or the class centers are estimated, all BMUs are transferred to the unfolded SOM. (A), Torus distance. To estimate the torus distance, all BMUs are mapped onto 9 identical grids. (B), Examples of BMUs in the original (top row) and unfolded (bottom row) SOMs. The columns show BMUs from CL1, CL2, CL3 and CL4, respectively. The class center is the center of BMUs' mass in the unfolded SOMs shown in the bottom row. It should be noted that SOMs in the bottom row are three times larger than the original SOMs in the top row.

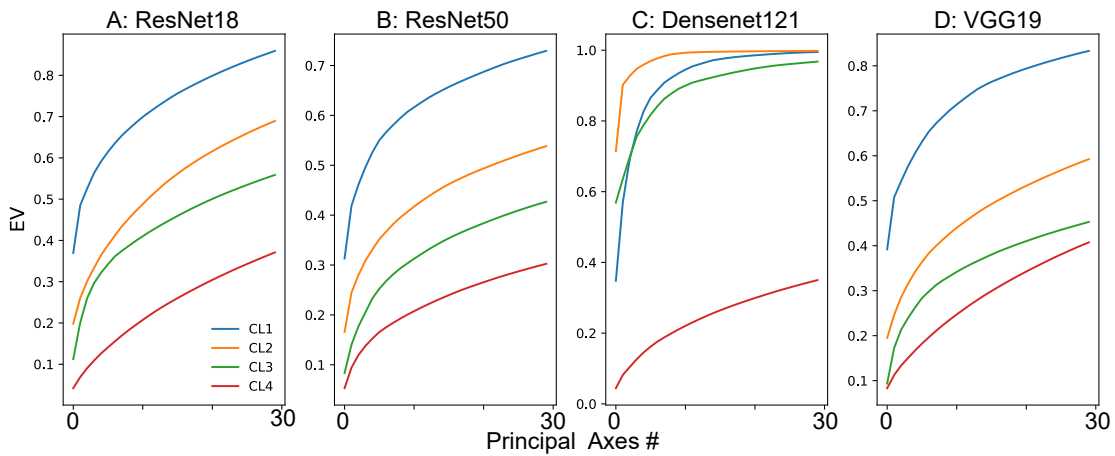


Figure 3: We conduct PCA analyses on vector codes from ResNet18 and display the explained variable (EV) in (A), Blue, orange, green and red line denote CL1, CL2, CL3 and CL4, respectively. EV measured from ResNet18's responses (vector codes) to SOM-tr (i.e., 50,000 examples from the ImageNet train set). (B)-(D), EVs are measured from ResNet50, Densenet121 and VGG19.

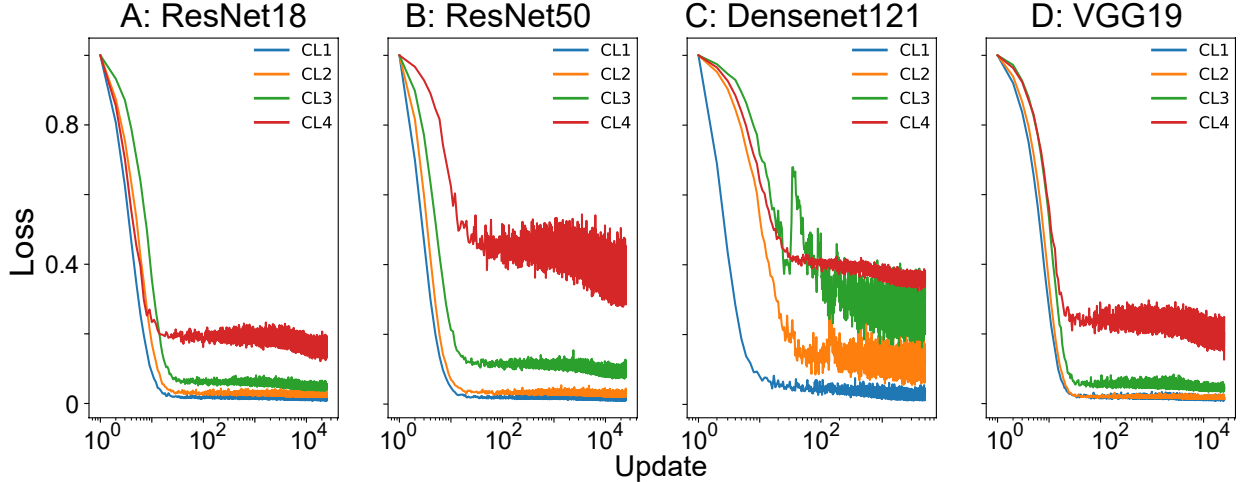


Figure 4: Loss function of SOMs trained on 4 models’ vector codes. Blue, orange, green and red line denote CL1, CL2, CL3 and CL4, respectively. (A)-(D), Time courses of SOM training of ResNet18, ResNet50, DenseNet121 and VGG19.

3.1 Analysis of functional codes

To further probe internal codes in hidden layers and their changes in DL models, we seek functional codes (functional codes) by training SOMs on vector codes from CL1, 2, 3 and 4. To obtain layer-specific functional codes, we train 4 individual SOMs on vector codes elicited by SOM-tr for 5 epochs. During training, we use 10 as a batch size for ResNet18, 50 and VGG19 and 50 for DenseNet121. If all inputs to SOMs are identical, only a single unit would be chosen as BMU, and its weight would approach the input rapidly. If inputs are diverse, more units would be chosen as BMUs to learn distinct inputs. When a sufficient number of units learn their inputs’ representations, SOMs cannot learn new inputs that are substantially different from previous ones, and thus, the loss function may remain a relatively high value. Conversely, we could expect the loss function of SOM to reflect the inputs’ diversity. With this possibility in mind, we evaluate the loss function during training. As shown in Fig. 4A, the loss functions of SOMs, trained on ResNet18’s vector codes, decline initially and then become saturated at different levels depending on layers. We also observe the equivalent results with ResNet50, DenseNet121 and VGG19 (Fig. 4B-D), supporting our PCA analysis that functional codes in shallow layers are homogeneous, but those in deep layers are diverse.

We then ask if the inputs are mapped onto a finite number of internal codes (i.e., functional codes) as in many-to-one like mappings. If multiple inputs are mapped onto the same code, they will be mapped onto the same ‘SOM unit’. Consequently, if the units in SOM encode important functional codes, they will be chosen as BMUs more frequently than others. Further, as similar inputs would be mapped onto neighboring BMUs, BMUs could be grouped together in an homogeneous fashion. With this possibility in mind, we estimate the densities of BMUs using Gaussian kernels [31] (Fig.5 and Supplementary Fig. 1). As shown in the figure, some units are chosen as BMUs more frequently than others.

This result supports that DL may map diverse inputs to a finite number of internal codes. Then, the question is, do these codes encode semantic meaning? If they are correlated, the inputs drawn from the same class could be mapped onto the neighboring BMUs. As shown in Fig. 6, BMUs of the same class inputs are clustered together. Notably, the spatial spreads of BMUs are relatively bigger in shallow layers but smaller in deep layers. Furthermore, we observe that SOM-val, which is not used to train SOMs, elicits a similar set of units (Fig. 6); we find equivalent results from SOM trained on ResNet50 (Supplementary Fig. 2). These results suggest that SOMs can learn semantically meaningful codes, and their correlations to the labels (i.e., classes) of inputs become stronger in deep layers.

To quantify this observation, we evaluate the Euclidean distance (D_{class}) between individual BMUs of the same class inputs and their centers. In doing so, we first identify the class center (i.e., the centroids of BMUs of the same class inputs) and calculate the D_{class} in the 2D torus (see section 2.4 and Fig. 2). In this analysis, we calculate the average distances on a class-by-class basis. Fig. 7A and B show the distributions of distances of all 1000 classes. As shown in the figure, the distances to the class centers are much smaller in deep layers than those in shallow layers. The distances measured by unseen examples (from ImageNet validation set) indicate the same trend. We also ask if D_{class} are correlated with ResNet’s answers and find that D_{class} is bigger when ResNet makes an incorrect prediction than when ResNet makes a correct prediction; see supplementary Text and Supplementary Fig. 3.

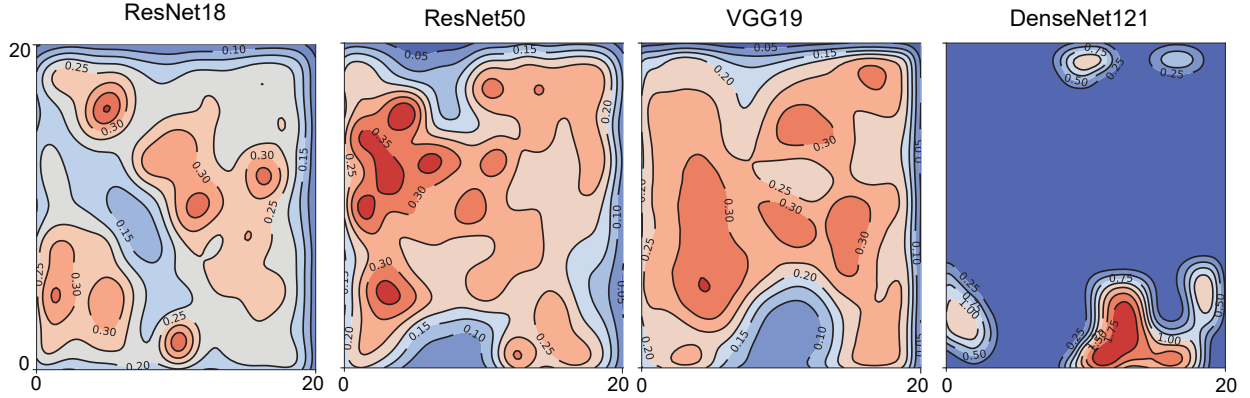


Figure 5: Density of BMUs. 4 panels show BMUs of ResNet18, ResNet50, VGG19 and DenseNet121, respectively. For the sake of brevity, we show BMUs of CL2 only. For all 4 layers, see Supplementary Fig. 1. We note that the density per area is very low. For illustration purpose only, we scale up the density by 100 times.

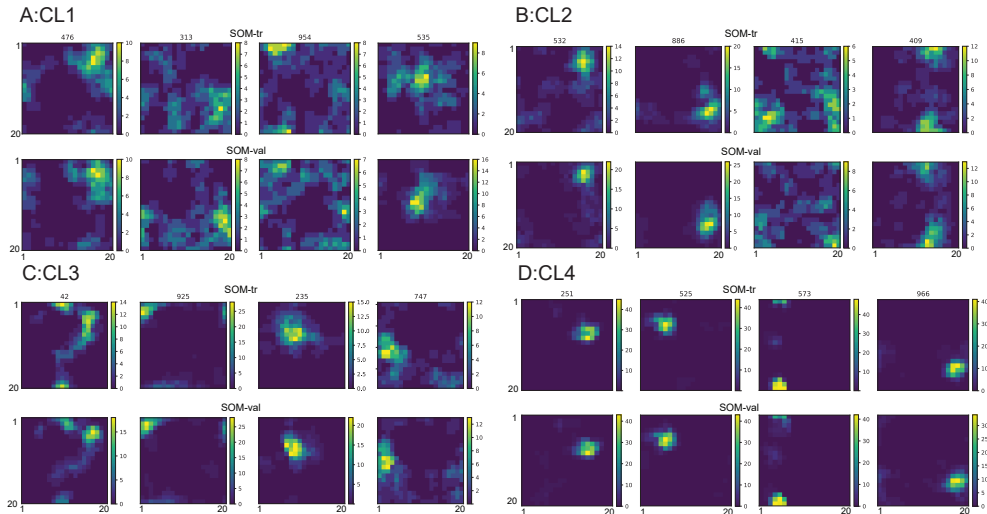


Figure 6: BMUs of vector codes of ResNet18. For each input, we collect vector codes from CL1-CL4 of ResNet18 and estimate their 10 BMUs in the trained SOM. (A), BMUs in CL1. (B), BMUs in CL2, (C), BMUs in CL3. (D), BMUs in CL4. The top panels show BMUs of examples in SOM-tr, which are used to train SOMs. The bottom panels show BMUs of examples in SOM-val, which are not used to train SOMs. Each column shows BMUs of inputs in the same class; the number above the panels denotes their class IDs in the ImageNet.

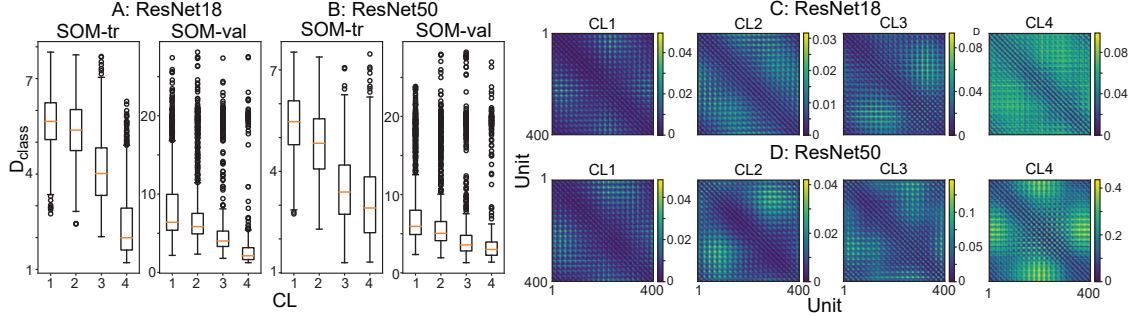


Figure 7: D_{class} , Euclidean distance, between individual BMUs to their class centers. For each ImageNet class, we first obtain the class center and calculate the mean distance between BMUs and the class center. To show the statistical properties of all 1000 classes, we use the box plot. (A), D_{class} measured in ResNet18 using SOM-tr (left) and SOM-val (right). The open circles denote outliers (i.e., classes significantly different from others). We observe outliers more frequently in SOM-val, which is not used to train SOMs. (B), D_{class} in ResNet50. (C), Cosine distance (Eq. 2) between the weights of SOMs trained on vector codes from 4 CLs of ResNet18. (D), Cosine distance between weights between SOMs trained on ResNet50. We display all pairs of 400 units in the 20-by-20 SOM.

These results suggest that inputs can be mapped onto a finite number of functional codes throughout ResNets and that SOMs can store them in their weights. With proxy functional codes, we ask how functional codes evolve over layers. Specifically, inspired by our PCA analysis suggesting that shallow layers have small intrinsic dimensions, we evaluate the homogeneity of functional codes in all 4 layers by calculating cosine distance (Eq. 2) between the functional codes (i.e., the weights of SOM) of ResNet18 and ResNet50. Interestingly, cosine distances between weights of SOM trained on CL1 are quite small, but they become bigger when SOMs are trained on deep layers (Fig. 7 C and D).

That is, the functional codes are homogeneous in shallow layers but diverse in deep layers. Furthermore, we evaluate the similarity between 100 pairs of class centers. Specifically, we identify the centers of BMUs obtained from SOM-tr and then evaluate the cosine distance between the selected 100 center BMUs’ weights in ResNet18, ResNet50, VGG19 and DenseNet121. Importantly, the cosine distances between class centers are small but become bigger in CL4 (Fig. 8).

To address if this observation is valid for other datasets, we repeat the same analysis with ResNet50 trained on CIFAR10, 100 [32] and SVHN [33] and find the equivalent results (Fig. 9). Further, we observe that the cosine distances between class centers are much closer to each other in CL1 and CL4 in all 4 ImageNet models and ResNet50 trained on CIFAR10, CIFAR100 and SVHN (Fig. 10).

In brief, these results raise the possibility that DL models map diverse inputs to a group of extremely homogeneous codes in shallow layers but more diverse codes in deep layers, leading us to hypothesize that DL relies on two types of adaptive mappings. First, it maps diverse inputs onto homogeneous codes, which occur in shallow layers. Second, it maps homogeneous codes in shallow layers mapping onto diverse codes in deeper layers.

3.2 A potential link between generalization ability and vulnerability to adversarial inputs and functional telescope hypothesis

Why does DL map inputs to homogeneous codes in shallow layers? We note that DL models’ responses (f) can be locally linear $f(x + \delta) = f(x) + f(\delta)$, when $\delta \rightarrow 0$. Let’s consider the decomposition $f = f_d \circ f_s$, where f_s and f_d represent mappings between input and shallow layers and between shallow and deep layers, respectively. With $f_s(x_i) = c_i$, we can get $f(x_i), f(x_j) = f_d(c_i), f_d(c_j)$. Our results above suggest that 1) c_i and c_j are similar in general and 2) that $\|c_i - c_j\|$ is smaller when x_i and x_j are drawn from the same class. Then, we can speculate that if x_i and x_j are drawn from the same class, $\|f(x_i) - f(x_j)\|$ will be readily small, which can make generalization easier.

However, this argument also suggests that DL models’ decisions could be easily flipped if there is an effective way to perturb c_i since c_i are similar to each other. Based on this possibility, we hypothesize the extremely homogeneous functional codes in shallow layers may explain DL models’ vulnerabilities to adversarial inputs. To address this hypothesis, we turn to adversarial perturbations known to change DL models’ predictions with minimal perturbations on inputs. Specifically, we evaluate the influence of adversarial inputs on functional codes in ResNet18 and ResNet50 by using SOM. As the distances between BMUs reflect the similarity between inputs, we measure the Euclidean distance between clean BMUs and adversarial BMUs. When adversarial perturbations change the functional codes significantly, the distance will be big. In this analysis, we also measure the influence of random perturbation as a control condition.

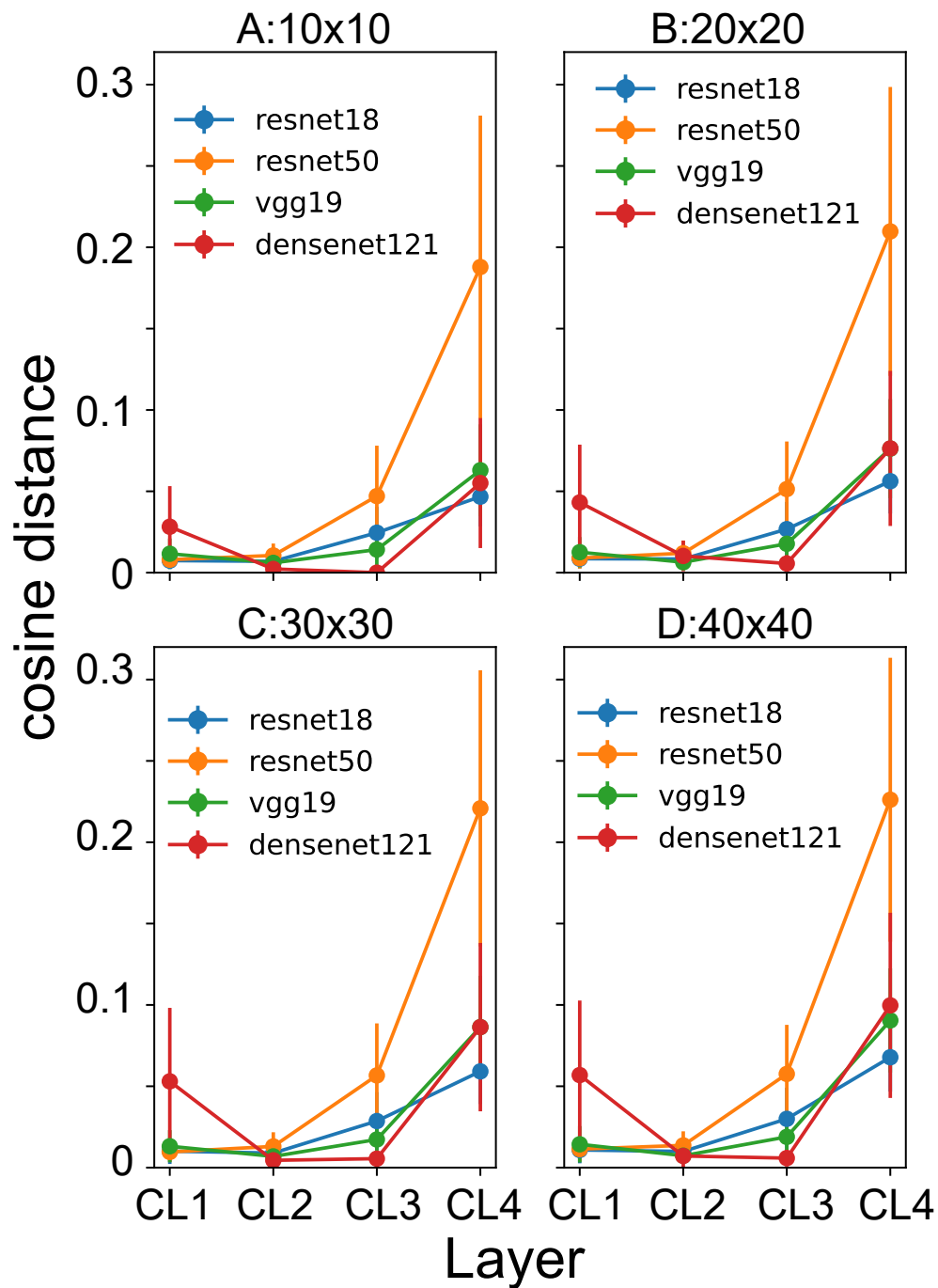


Figure 8: Cosine distance between class centers' weights in all 4 layers. We measure cosine distances from SOMs with 10×10 , 20×20 , 30×30 and 40×40 nodes, and they are shown in (A)-(D), respectively. In each panel, the color denotes the model analyzed.

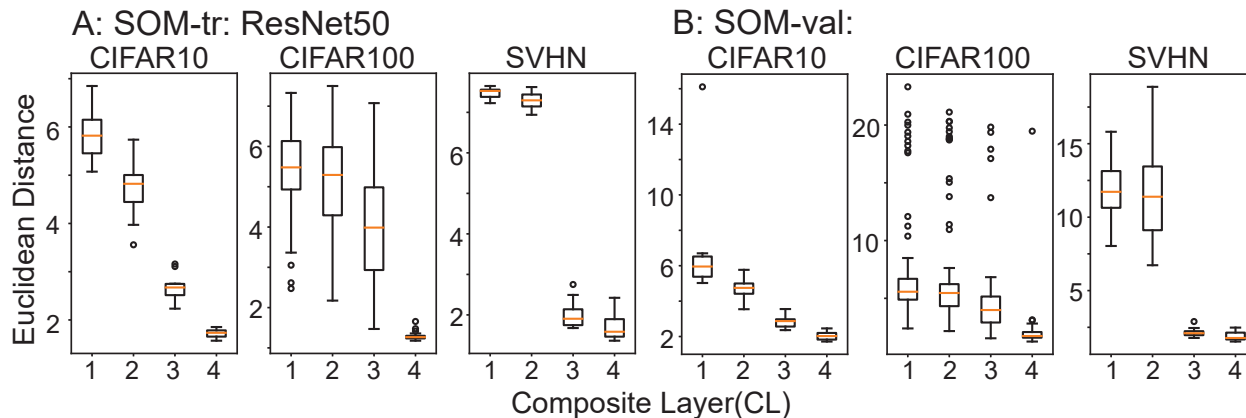


Figure 9: Euclidean distance between individual BMUs to their class centers when ResNet50 is trained on CIFAR10, CIFAR100 and SVHN. (A), Euclidean distance to class centers when training examples are tested. (B), Euclidean distance to class centers when test examples are tested.

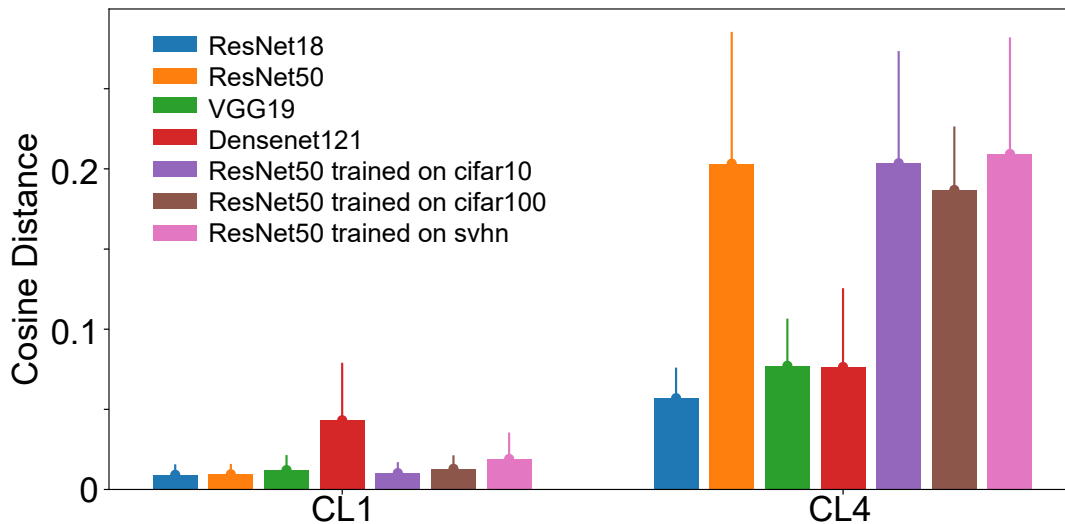


Figure 10: Cosine Distance between class centers' weights. We display distances between the centers of 100 classes randomly chosen in CL1 and CL4.

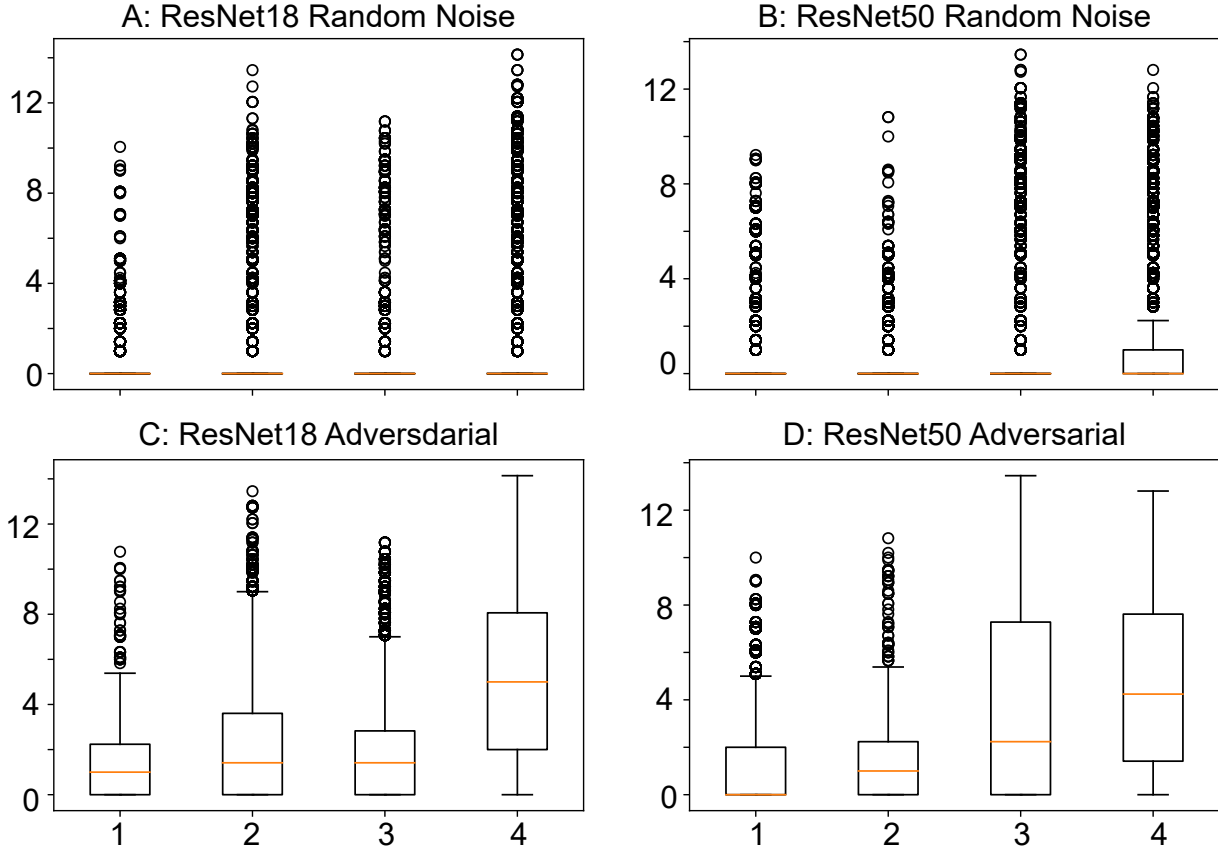


Figure 11: Influence of adversarial and random perturbations on functional codes in ResNets. We measure the Euclidean distance between clean BMUs and perturbed BMUs. For each pair of clean and perturbed inputs, we record 10 BMUs from both images and calculate Euclidean distance. (A), Euclidean distance between clean and random noise BMUs when ResNet18 is analyzed. (B), the same as (A) but the model is ResNet50. (C), Euclidean distance between clean and adversarial inputs when ResNet18 is analyzed. (D), the same as (C) but the model is ResNet50.

We randomly choose 500 images from ImageNet and perturb them using projected gradient attack (PGD) [34] and an open-source adversarial attack library [35]. We restrain perturbation strength ϵ to be smaller than $1/255$; see Table 2 for other hyperparameters used in the experiment. Random noises, as a control condition, are added to the same 500 images and are independently drawn from a uniform distribution between 0 and $1/255$. Although the magnitudes of adversarial and random perturbations are comparable, their influences on ResNet18 and 50 are strikingly different. ResNet18 and 50 prediction accuracy drops from 77.8% and 93.0 % to 3.6% and 6.6%, respectively, whereas random noises do not change the models’ prediction accuracy (77.8% and 93.0 %). For each pair of clean and perturbed images,

Table 2: Parameters used to craft adversarial images.

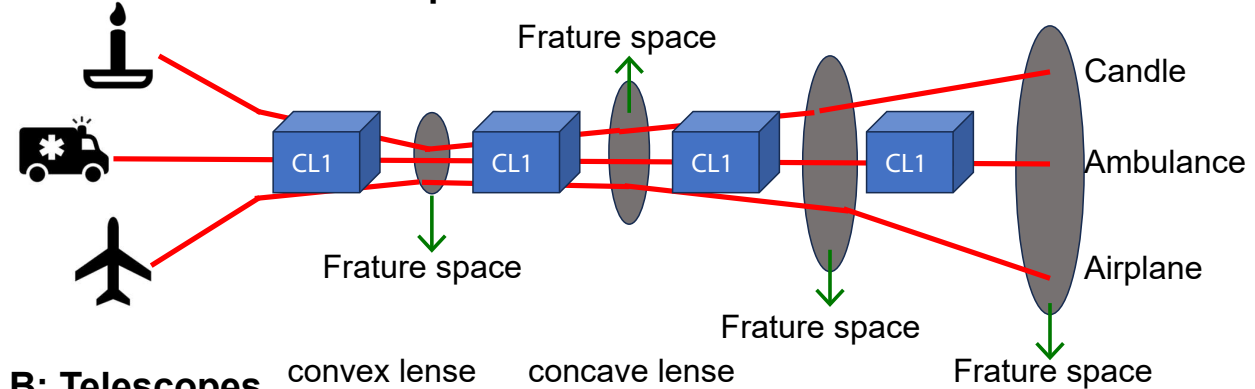
Arguments (name in advtorch)	Value
Loss function (loss_fn)	CrossEntropyLoss
Maximum perturbation (eps, ϵ)	$\frac{1}{255}$
Iteration (nb_iter)	50
Update step size (eps_iter)	$\frac{1}{255} \times \frac{2}{100}$
rand_int	True
targeted	False
clip_min	0.0
clip_max	1.0
norm	L_{inf}

we obtain 10 best BMUs from both clean and perturbed images. Figs. 11 A and B show the distances between 10

pairs of BMUs elicited by clean and random noise inputs. As shown in the figures, random noise inputs do not have substantial influence on all 4 layers. By contrast, adversarial inputs do change the functional codes in all 4 layers, but in significantly different degrees. In CL1, the distances observed are very small, but they are noticeably bigger in CL4. This is consistent with an earlier analysis [36] that utilizes UMAP to compare clean and adversarial inputs, but it is still surprising, since the responses of CL2-4 entirely depend on CL1.

Inspired by our two observations that functional codes in shallow layers are homogeneous (Figs. 7, 8, 10), and that adversarial attacks use small perturbations in shallow layers to induce strong perturbations in functional codes in deeper layers (Fig. 11), we propose our functional telescope hypothesis that DL uses shallow layers to map high-dimensional inputs into extremely homogeneous codes and use deeper layers to gradually convert them into decision variables central for accurate predictions on the class of inputs. Fig. 12 summarizes our hypothesis, and we argue that this hypothesis can explain that small perturbations producing significant influences in deeper layers.

A: DL models' feature space



B: Telescopes

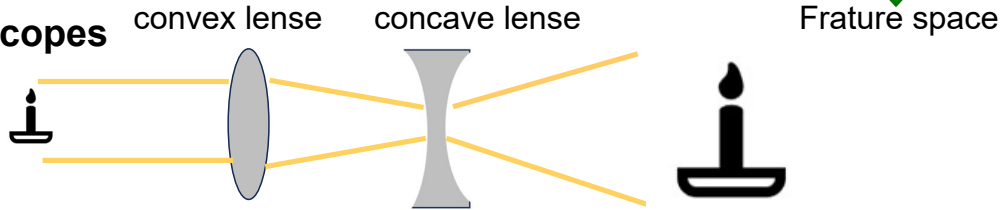


Figure 12: Functional Telescope Hypothesis proposes that feature spaces of DL models are condensed and then expanded.

4 Discussion

Based on our results, we propose that DNNs' operations closely resemble a telescope's operations. The compressed feature space, in which all features/codes are homogeneous, may be a double-edged sword which readily enables generalization ability but creates DNNs' vulnerabilities to adversarial perturbations.

4.1 Links to earlier works

Producing generalizations is one of DNNs' key capabilities, and an earlier study suggested that their vulnerabilities to adversarial perturbations are connected to the generalization of non-essential features [37]. Our analyses are consistent with their finding and further suggest that such erroneous generalization can easily occur due to compressed feature space. The model stitching [38] suggested that shallow layers from more powerful DNNs can boost less powerful DNNs' performance. Our functional telescope hypothesis suggest that shallow layers shallow layers' essential function is to create condensed feature space, and thus, shallow layers may be exchangeable between models, which can explain why model stitching is possible.

4.2 Limitation and future extension of our analysis

In this study, we analyze popular convolutional networks. However, transformers [39] do not rely on convolution but rely on attentional heads and fully connected layers. Our results will likely hold for modern convolutional networks, but

it remains unclear if our functional telescope hypothesis can explain transformers’ operations. Furthermore, we use a simple coding rule to describe feature maps’ responses to analyze DL models’ internal representations more quickly with limited computing resources, which may not be powerful enough to fully capture feature maps’ information. In the future, we will expand our analysis to non-convolutional architecture such as transformers and recurrent networks and explore optimal coding rules that can efficiently describe feature maps.

References

- [1] Yann Lecun, Yoshua Bengio, and Geoffrey Hinton. Deep learning. *Nature*, 521(7553):436–444, 2015. ISSN 14764687. doi:10.1038/nature14539.
- [2] Ajay Shrestha and Ausif Mahmood. Review of deep learning algorithms and architectures. *IEEE Access*, 7: 53040–53065, 2019. doi:10.1109/ACCESS.2019.2912200.
- [3] Saptarshi Sengupta, Sanchita Basak, Pallabi Saikia, Sayak Paul, Vasilios Tsalavoutis, Frederick Atiah, Vadlamani Ravi, and Alan Peters. A review of deep learning with special emphasis on architectures, applications and recent trends. *Knowledge-Based Systems*, 194:105596, 2020. ISSN 0950-7051. doi:https://doi.org/10.1016/j.knosys.2020.105596. URL https://www.sciencedirect.com/science/article/pii/S095070512030071X.
- [4] Zachary C. Lipton. The Mythos of Model Interpretability. In *ICML WHI*, 2016. ISBN 1539-3755 (Print). doi:10.1145/3233231. URL http://arxiv.org/abs/1606.03490.
- [5] Cynthia Rudin. Please Stop Explaining Black Box Models for High Stakes Decisions. In *NIPS Workshop*, 2018. ISBN 1811.10154v2. doi:arXiv:1811.10154v2. URL http://arxiv.org/abs/1811.10154.
- [6] Christian Szegedy, Wojciech Zaremba, Ilya Sutskever, Joan Bruna, Dumitru Erhan, Ian Goodfellow, and Rob Fergus. Intriguing properties of neural networks, 2013. URL https://arxiv.org/abs/1312.6199.
- [7] Anirban Chakraborty, Manaar Alam, Vishal Dey, Anupam Chattopadhyay, and Debdeep Mukhopadhyay. Adversarial attacks and defences: A survey, 2018. URL https://arxiv.org/abs/1810.00069.
- [8] Xiaoyong Yuan, Pan He, Qile Zhu, and Xiaolin Li. Adversarial examples: Attacks and defenses for deep learning. *IEEE Transactions on Neural Networks and Learning Systems*, 30(9):2805–2824, 2019. doi:10.1109/TNNLS.2018.2886017.
- [9] Chris Olah, Alexander Mordvintsev, and Ludwig Schubert. Feature visualization. *Distill*, 2017. doi:10.23915/distill.00007. https://distill.pub/2017/feature-visualization.
- [10] Matthew D. Zeiler and Rob Fergus. Visualizing and understanding convolutional networks. *CoRR*, abs/1311.2901, 2013. URL http://arxiv.org/abs/1311.2901.
- [11] Shan Carter, Zan Armstrong, Ludwig Schubert, Ian Johnson, and Chris Olah. Activation atlas. *Distill*, 2019. doi:10.23915/distill.00015. https://distill.pub/2019/activation-atlas.
- [12] Bruno Olshausen and David Field. Emergence of simple-cell receptive field properties by learning a sparse code for natural images. *Nature*, 381:607–9, 07 1996. doi:10.1038/381607a0.
- [13] Ramprasaath R. Selvaraju, Michael Cogswell, Abhishek Das, Ramakrishna Vedantam, Devi Parikh, and Dhruv Batra. Grad-CAM: Visual explanations from deep networks via gradient-based localization. *International Journal of Computer Vision*, 128(2):336–359, oct 2019. doi:10.1007/s11263-019-01228-7. URL https://doi.org/10.1007%2Fs11263-019-01228-7.
- [14] Mukund Sundararajan, Ankur Taly, and Qiqi Yan. Axiomatic attribution for deep networks. In Doina Precup and Yee Whye Teh, editors, *Proceedings of the 34th International Conference on Machine Learning*, volume 70 of *Proceedings of Machine Learning Research*, pages 3319–3328. PMLR, 06–11 Aug 2017. URL https://proceedings.mlr.press/v70/sundararajan17a.html.
- [15] Marco Ancona, Enea Ceolini, Cengiz Öztireli, and Markus Gross. Towards better understanding of gradient-based attribution methods for deep neural networks. In *International Conference on Learning Representations*, 2018. URL https://openreview.net/forum?id=Sy21R9JAW.
- [16] Grégoire Montavon, Alexander Binder, Sebastian Lapuschkin, Wojciech Samek, and Klaus-Robert Müller. *Layer-Wise Relevance Propagation: An Overview*, pages 193–209. Springer International Publishing, Cham, 2019. ISBN 978-3-030-28954-6. doi:10.1007/978-3-030-28954-6_10. URL https://doi.org/10.1007/978-3-030-28954-6_10.
- [17] Chris Olah, Alexander Mordvintsev, and Ludwig Schubert. Feature visualization. *Distill*, 2017. doi:10.23915/distill.00007. https://distill.pub/2017/feature-visualization.

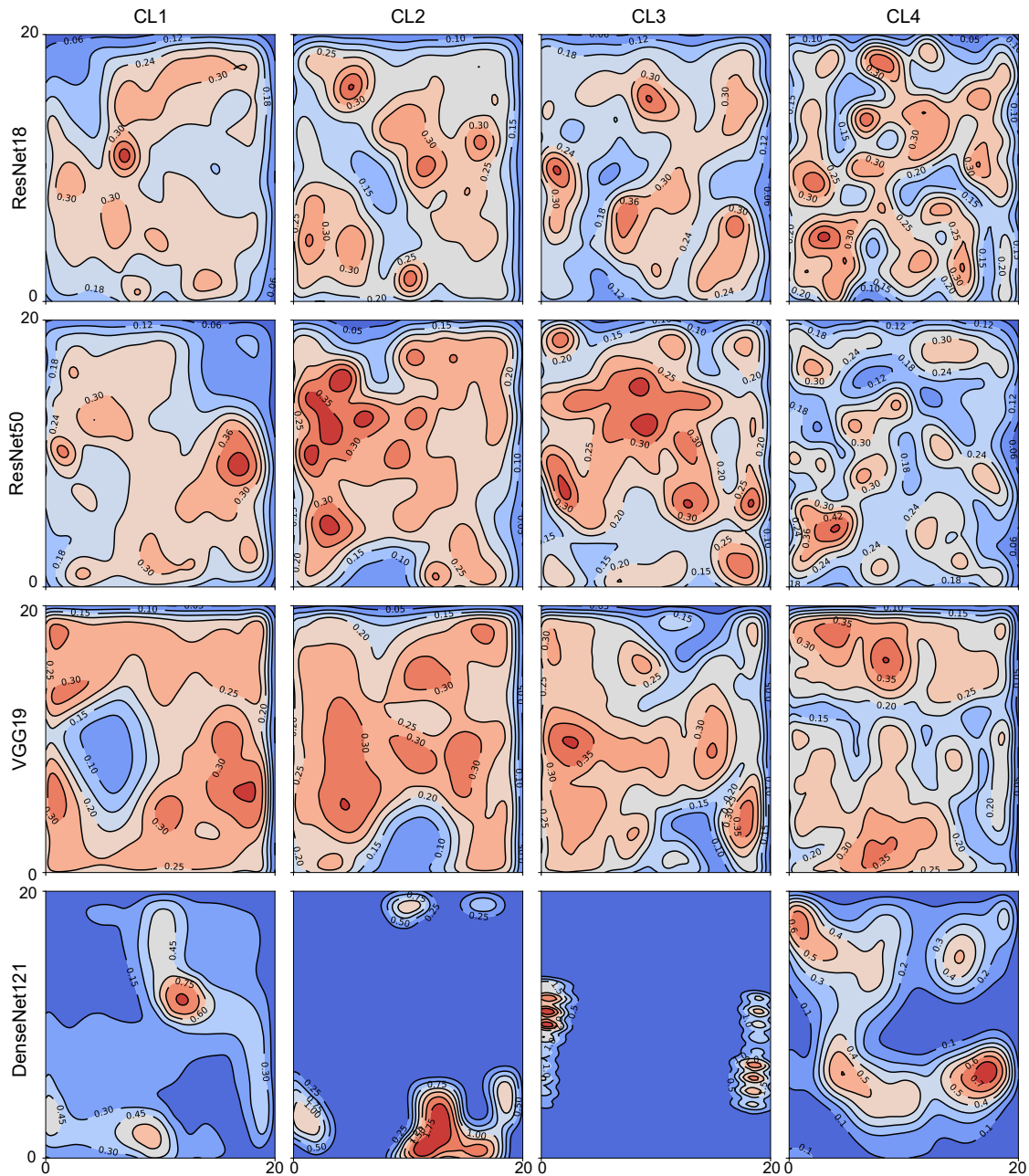
- [18] Been Kim, Martin Wattenberg, Justin Gilmer, Carrie Cai, James Wexler, Fernanda Viegas, and Rory sayres. Interpretability beyond feature attribution: Quantitative testing with concept activation vectors (TCAV). In Jennifer Dy and Andreas Krause, editors, *Proceedings of the 35th International Conference on Machine Learning*, volume 80 of *Proceedings of Machine Learning Research*, pages 2668–2677. PMLR, 10–15 Jul 2018. URL <https://proceedings.mlr.press/v80/kim18d.html>.
- [19] Guillaume Alain and Yoshua Bengio. Understanding intermediate layers using linear classifier probes, 2018.
- [20] Jung Hoon Lee. Library network, a possible path to explainable neural networks, 2019. URL <https://arxiv.org/abs/1909.13360>.
- [21] T. Kohonen. The self-organizing map. *Proceedings of the IEEE*, 78(9):1464–1480, 1990. doi:10.1109/5.58325.
- [22] T. Kohonen and T. Honkela. Kohonen network. *Scholarpedia*, 2(1):1568, 2007. doi:10.4249/scholarpedia.1568. revision #127841.
- [23] Archit Rathore, Nithin Chalapathi, Sourabh Palande, and Bei Wang. Topoact: Visually exploring the shape of activations in deep learning, 2021.
- [24] Emilie Purvine, Davis Brown, Brett Jefferson, Cliff Joslyn, Brenda Praggastis, Archit Rathore, Madelyn Shapiro, Bei Wang, and Youjia Zhou. Experimental observations of the topology of convolutional neural network activations, 2022.
- [25] Kaiming He, Xiangyu Zhang, Shaoqing Ren, and Jian Sun. Deep residual learning for image recognition, 2015. URL <https://arxiv.org/abs/1512.03385>.
- [26] Gao Huang, Zhuang Liu, Laurens van der Maaten, and Kilian Q. Weinberger. Densely connected convolutional networks, 2018.
- [27] Karen Simonyan and Andrew Zisserman. Very deep convolutional networks for large-scale image recognition. In *International Conference on Learning Representations*, 2015.
- [28] Ross Wightman. Pytorch image models. <https://github.com/rwightman/pytorch-image-models>, 2019.
- [29] Jia Deng, Wei Dong, Richard Socher, Li-Jia Li, Kai Li, and Li Fei-Fei. Imagenet: A large-scale hierarchical image database. In *2009 IEEE conference on computer vision and pattern recognition*, pages 248–255. Ieee, 2009.
- [30] Vincent Mallet, Michael Nilges, and Guillaume Bouvier. quicksom: Self-Organizing Maps on GPUs for clustering of molecular dynamics trajectories. *Bioinformatics*, 37(14):2064–2065, 11 2020. ISSN 1367-4803. doi:10.1093/bioinformatics/btaa925. URL <https://doi.org/10.1093/bioinformatics/btaa925>.
- [31] Pauli Virtanen, Ralf Gommers, Travis E. Oliphant, Matt Haberland, Tyler Reddy, David Cournapeau, Evgeni Burovski, Pearu Peterson, Warren Weckesser, Jonathan Bright, Stéfan J. van der Walt, Matthew Brett, Joshua Wilson, K. Jarrod Millman, Nikolay Mayorov, Andrew R. J. Nelson, Eric Jones, Robert Kern, Eric Larson, C J Carey, İlhan Polat, Yu Feng, Eric W. Moore, Jake VanderPlas, Denis Laxalde, Josef Perktold, Robert Cimrman, Ian Henriksen, E. A. Quintero, Charles R. Harris, Anne M. Archibald, Antônio H. Ribeiro, Fabian Pedregosa, Paul van Mulbregt, and SciPy 1.0 Contributors. SciPy 1.0: Fundamental Algorithms for Scientific Computing in Python. *Nature Methods*, 17:261–272, 2020. doi:10.1038/s41592-019-0686-2.
- [32] Alex Krizhevsky, Geoffrey Hinton, et al. Learning multiple layers of features from tiny images. 2009.
- [33] Yuval Netzer, Tao Wang, Adam Coates, Alessandro Bissacco, Bo Wu, and Andrew Y Ng. Reading digits in natural images with unsupervised feature learning. 2011.
- [34] Aleksander Madry, Aleksandar Makelov, Ludwig Schmidt, Dimitris Tsipras, and Adrian Vladu. Towards deep learning models resistant to adversarial attacks, 2017. URL <https://arxiv.org/abs/1706.06083>.
- [35] Gavin Weiguang Ding, Luyu Wang, and Xiaomeng Jin. AdverTorch v0.1: An adversarial robustness toolbox based on pytorch. *arXiv preprint arXiv:1902.07623*, 2019.
- [36] Gabriel D. Cantareira, Rodrigo F. Mello, and Fernando V. Paulovich. Explainable adversarial attacks in deep neural networks using activation profiles, 2021. URL <https://arxiv.org/abs/2103.10229>.
- [37] Andrew Ilyas, Shibani Santurkar, Dimitris Tsipras, Logan Engstrom, Brandon Tran, and Aleksander Madry. Adversarial examples are not bugs, they are features. In H. Wallach, H. Larochelle, A. Beygelzimer, F. d'Alché-Buc, E. Fox, and R. Garnett, editors, *Advances in Neural Information Processing Systems*, volume 32. Curran Associates, Inc., 2019. URL https://proceedings.neurips.cc/paper_files/paper/2019/file/e2c420d928d4bf8ce0ff2ec19b371514-Paper.pdf.
- [38] Yamini Bansal, Preetum Nakkiran, and Boaz Barak. Revisiting model stitching to compare neural representations. In A. Beygelzimer, Y. Dauphin, P. Liang, and J. Wortman Vaughan, editors, *Advances in Neural Information Processing Systems*, 2021. URL <https://openreview.net/forum?id=ak06J5jNR4>.

- [39] Jacob Devlin, Ming-Wei Chang, Kenton Lee, and Kristina Toutanova. BERT: pre-training of deep bidirectional transformers for language understanding. In Jill Burstein, Christy Doran, and Thamar Solorio, editors, *Proceedings of the 2019 Conference of the North American Chapter of the Association for Computational Linguistics: Human Language Technologies, NAACL-HLT 2019, Minneapolis, MN, USA, June 2-7, 2019, Volume 1 (Long and Short Papers)*, pages 4171–4186. Association for Computational Linguistics, 2019. doi:10.18653/v1/n19-1423. URL <https://doi.org/10.18653/v1/n19-1423>.

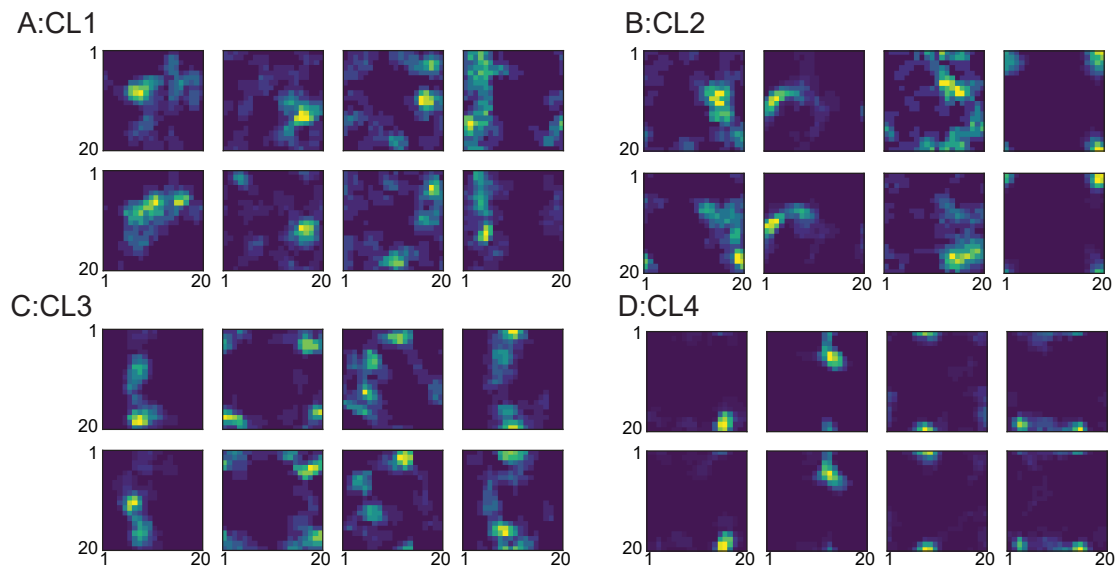
Supplemental Text

We test if ResNets utilize functional codes for decision-making by estimating the correlations between functional codes and ResNets' decisions. In this test, we group functional codes depending on whether ResNets make correct predictions of the inputs' labels. If functional codes are linked to ResNets' decisions, BMUs storing functional codes would be close to the centers of the class predicted by ResNets. If this assumption holds, when ResNets make correct predictions, BMUs storing functional codes would be close to the centers of the labels. By contrast, when ResNets make incorrect predictions, they would be close to the centers of the classes different from the labels. Based on this line of thought, we expect the distance (Euclidean distance, ED) between BMUs and the label centers to be bigger when ResNets' make incorrect predictions than when they make correct predictions. In the analysis, we estimate the centers of the labels using SOM-tr and test ED between BMUs and the label centers using SOM-val; this is consistent with other analyses, in which the class centers are estimated using SOM-tr only. As shown in Supplemental Fig. 3, ED is bigger on average when ResNets make mistakes.

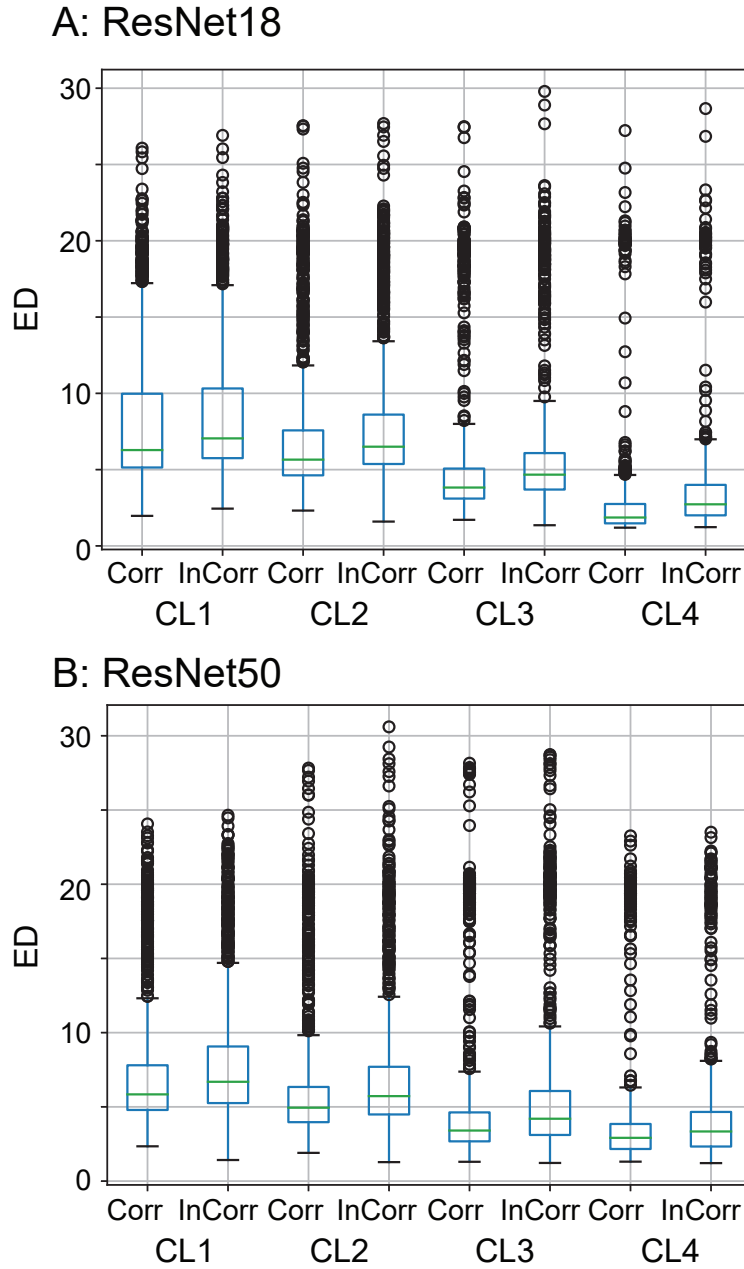
Supplemental Figures



Supplementary Figure 1: Density of BMUs. Four rows show BMUs of ResNet18, ResNet50, VGG19 and DenseNet121, respectively. Each column shows BMUs from one of 4 CLs (see the name of CL shown above the column). We note that the density per area is very low. For illustration purpose only, we scaled the density by 100 times.



Supplementary Figure 2: BMUs of vector codes obtained from ResNet50. The panels show BMUs of SOMs trained on ResNet50. (A), BMUs of vector codes in CL1. The top row shows the BMUs of SOM-tr, whereas the bottom row shows the BMUs of SOM-val. Each column shows BMUs of the inputs in the same class. (B), the same as (A), but vector codes were obtained from CL2. (C), the same as (A), but vector codes were obtained from CL3.(D), the same as (A), but vector codes were obtained from CL4.



Supplementary Figure 3: EDs between BMUs and the label centers. For each class, we estimate the mean ED over 50 examples from SOM-val; we consider 10 BMUs per input. The label centers are estimated using SOM-tr. x -axis denotes the data type. EDs are grouped based on CL and whether ResNets make correct predictions (Corr) or not (InCorr). The open circles in the plots denote the outlier classes. (A), EDs measured from SOMs trained on ResNet18. (B), EDs measured from SOMs trained on ResNet50.